Characterizing the Transition to Irrecoverable Deformation in the Subsurface with an InSAR Multi-Sensor Time Series Analysis

Sayyed Mohammad Javad Mirzadeh[1,2], Shuanggen Jin[1,3], Estelle Chaussard[4], Roland Bürgmann[5], Saba Ghotbi[6], and Andreas Braun[7]

[1] Shanghai Astronomical Observatory, Chinese Academy of Sciences, Shanghai 200030, China

[2] School of Astronomy and Space Science, University of Chinese Academy of Sciences, Beijing 100049, China

[3] School of Surveying and Land Information Engineering, Henan Polytechnic University, Jiaozuo 454000, China

[4] Independent Researcher

[5] Department of Earth and Planetary Science, University of California Berkeley, Berkeley, CA 94720-4767, USA

[6] Singhofen and Associates Incorporated, 11723 Orpington St., Orlando, FL 32817, USA

[7] Department of Geography, University of Tübingen, 72070 Tübingen, Germany

Corresponding author: sgjin@shao.ac.cn; sg.jin@yahoo.com (S. Jin)

Key Points:

- This work provides a new method for tracking the onset of inelastic deformation in aquifer systems.
- In less than two decades, the Abarkuh Plain saw a rapid expansion of areas experiencing inelastic deformation due to groundwater extraction.
- InSAR time series post-processing enables isolating various sources contributing to the ground deformation and their relative importance.

Abstract

Tracking the onset of inelastic (permanent) deformation is critical to quantifying the stress experienced by an aquifer system so that the effects of current groundwater extraction practices are put in the context of the sedimentary and geological histories of a region. However, the pre-consolidation stress is rarely known due to the lack of multi-decadal ground-based data. In this paper, we propose a new approach to track the onset and spatial evolution of inelastic deformation based on a 2003-2020 multi-sensor Interferometric Synthetic Aperture Radar time series analysis. Our study reveals that in central Iran, many locations that used to experience elastic (recoverable) deformation just a few years ago, are now deforming inelastically, leading to irreversible lowering of the ground surface and irreversible loss of aquifer storage. Lithologic data reveals that the total thickness of the drained clay layers controls the extent and timing of the observed inelastic deformation, while groundwater data confirms that the multi-decadal lowering of groundwater levels is driving the long-term compaction. These results highlight that we are now at or near a tipping point in time between sustainability and permanent damage to our underground water resources, emphasizing the fact that current decisions have the potential to change the natural resources landscape permanently.

Plain Language Summary

Unsustainable extraction of groundwater is accompanied by irreversible land subsidence, the lowering of the ground surface elevation. Tracking the onset of inelastic (permanent) deformation is critical to isolating a tipping point in time between sustainability and permanent damage to our underground water resources. In this work, we present a new method based on space geodesy that enables quantifying the onset and spatial evolution of the inelastic ground deformation. Our study reveals that in central Iran, many locations that used to experience elastic (recoverable) ground deformation just a few years ago, are now deforming inelastically, leading to irreversible lowering of the ground surface and irreversible loss of aquifer storage. We find that while irreversible compaction is associated with multi-decadal groundwater levels decline, the nature and thickness of sediments in the subsurface relative to the local groundwater elevation control its timing. These results highlight the fact that recent and current groundwater management decisions have the potential to change the natural resources landscape permanently in central Iran.

1 Introduction

Interferometric Synthetic Aperture Radar (InSAR) is used to quantify ground deformation over small to very large areas worldwide (tens to thousands of square kilometers) with a high- spatial resolution (tens of meters) (Pepe and Calò, 2017). Ground deformation linked to subsurface and solid-earth processes has been precisely measured with InSAR and explored to gain insights into the physical and hydro-mechanical processes at play (e.g., Bürgmann et al. (2000)). InSAR has been broadly applied to the field of hydrology to derive the properties of aquifer systems and to guide water-storage management plans (Amelung et al., 1999; Chaussard et al., 2021; Ezquerro et al., 2014; Lu and Danskin, 2001; Miller and Shirzaei, 2015; Rezaei and Mousavi, 2019).

In an aquifer system, both inelastic (irreversible) and elastic (recoverable) deformation take place (Wilson and Gorelick, 1996), relating to hydraulic head fluctuations, properties of deforming sediment layers, and the aquifer's compaction history (Poland and Ireland, 1988). As long as the hydraulic head remains above the previous lowest level (i.e., the effective stress is less than the pre-consolidation stress), elastic deformation happens in the semi-permeable (sandy) layers. In contrast, when the hydraulic head falls below its previous lowest level, inelastic compaction takes place through the rearrangement of solid grains in clays (Guzy and Malinowska, 2020), which have an elastic compressibility one to three orders of magnitude lower than that the aquifers (Pavelko, 2004; Riley, 1998). Since inelastic and elastic processes often simultaneously happen at the same place, their separation is a challenging task without relying upon hydrological models (Hoffmann et al., 2003). However, quantifying these deformation components is essential to define sustainable pumping rates for resources management and to potentially relocate infrastructures from areas experiencing inelastic deformation (Shi et al., 2012).

Ojha et al. (2019) studied vertical land motion in the Central Valley, CA, with 2015-2017 InSAR time series and used a functional curve fitting to isolate elastic from inelastic contributions, assuming the elastic component to be seasonal. Chaussard et al. (2014) and Chaussard et al. (2017) explored land deformation in the Santa Clara aquifer, CA, and showed that elastic deformation can be spatiotemporally complex and reach amplitudes of centimeters each year. Using an Independent Component Analysis (ICA) of Sentinel-1 InSAR time series,

Mirzadeh et al. (2021) and Chaussard et al. (2021) highlighted the details of inelastic and elastic deformation signals in the Yazd-Ardakan Plain, Iran and in Mexico City, respectively. At both sites, deformation was shown to be dominantly inelastic and controlled by the thickness of clay-layers that compact as water levels drop below previous lowest stands. Gualandi and Liu (2021) applied a variational Bayesian ICA (vbICA) to 2015-2019 Sentinel-1 time series spanning the Central San Andreas Fault and southern Central Valley to isolate the contributions of deep and shallow aquifer deformation to the surface displacements and to separate tectonic loading from seasonal signals.

Since historical SAR missions (ERS1&2, Envisat, and ALOS-1) have a lower temporal sampling (35 to 46 days repeat) than the currently operating the Sentinel-1 satellite (6 to 12 days repeat), previous studies of elastic and inelastic deformations have mostly relied on the Sentinel-1 dataset, which limits the analysis to the short-term deformation (2014-now). Here, we introduce a method to extract the time-dependent evolution of inelastic deformation through consideration of a multi-sensor time series analysis of the historical and current SAR data combined with an ICA. We applied this method to InSAR time series of land deformation in the Abarkuh Plain (AP), Iran and resolved the primary control(s) by the geological and hydrological parameters to the spatially variable onset of inelastic deformation.

2 Abarkuh Plain

The AP is a desert extending from 52.67 to 53.72 E longitude and 30.68 and 31.50 N latitude. Its elevation ranges from 1439 m in the Abarkuh Playa in the southeast to 3277 m in the mountains to the west (Figure 1a). According to 1967-2011 data, the AP has an average annual rainfall of ~ 464.6 million m^3 and an annual evaporation of ~ 377.78 million m^3 (TAMAB, 2004). The AP unconfined aquifer covers an area of 929.12 km^2 (Figure 1a) and has suffered from an average yearly decline of groundwater levels of ~ 0.62 m between 1983 and 2017 (TAMAB, 2004). The long-term (1981-2011) groundwater balance in the AP aquifer indicates that the main recharge arises from the infiltration and return of wastewater from the agricultural sector at 61.1 million m^3 per year. Drawing by springs, qanats, and pumping wells account for 173.7 million m^3 per year, with the largest usage stemming from the agricultural sector with 168.1 million m^3 per year (Tables S1 and S2). The net yearly storage loss of 32.4 million m^3 has

led the local government to label the AP aquifer as the second-most imperiled aquifer in the Yazd province (TAMAB, 2004).

Figure 1a illustrates the geology of the AP. Quaternary sediments cover much of the area, consisting of alluvium (clays, silts, and sand along with gypsum) and salt flats. These Quaternary layers are overlaying Tertiary to Permian limestone and dolomite units (Figure 1b).

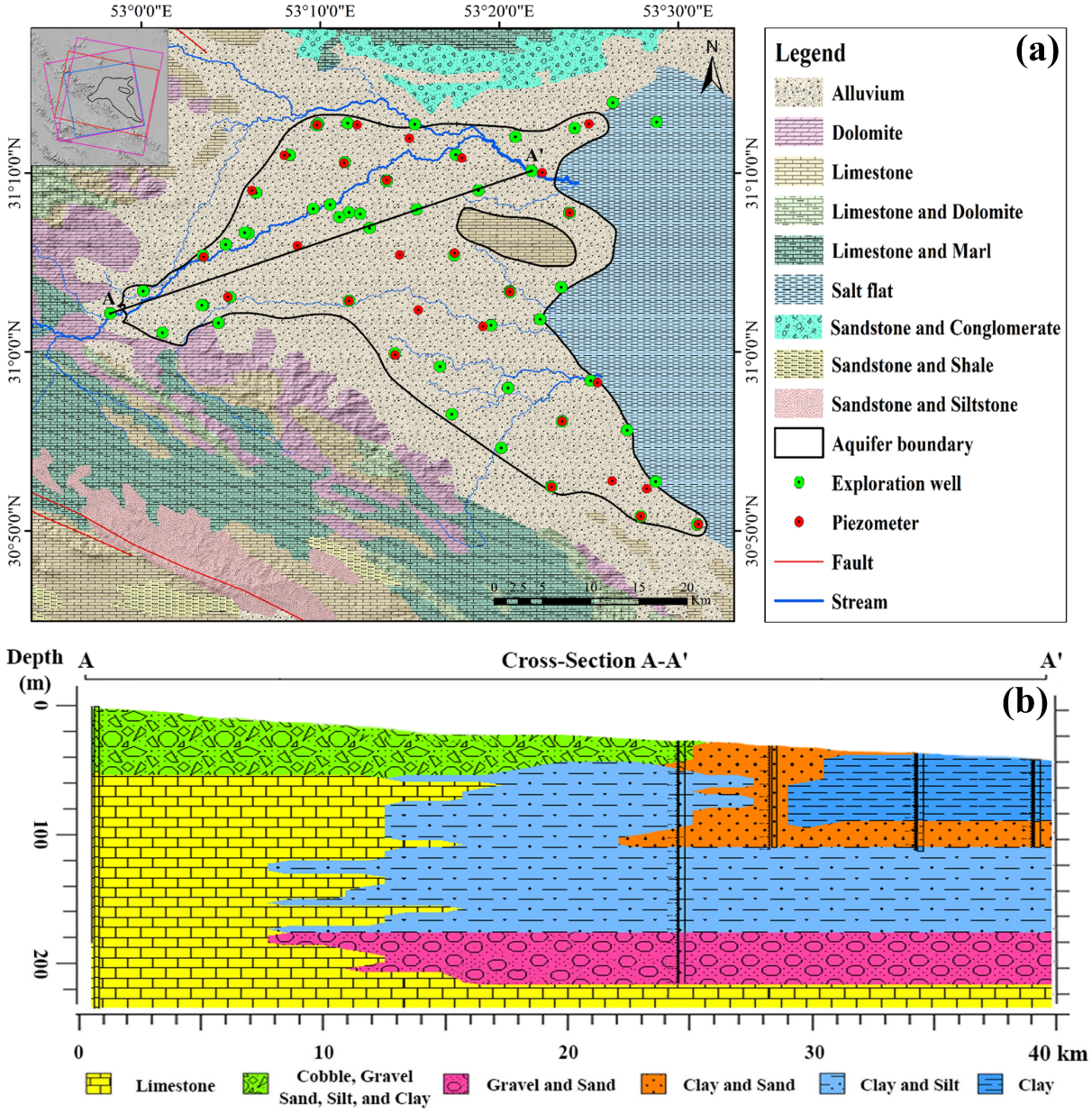

Figure 1. (a) Geological map of the AP. Black outlines denote the unconfined aquifer boundary. Green and red dots show the locations of exploration wells and piezometers, respectively, and the A-A' line displays the location of SW-NE cross-section. The inset shows outlines of frames from the Envisat descending, ALOS-1 ascending, and Sentinel-1 descending and ascending orbit directions in red, blue, and pink, respectively, overlaying a hillshade map. (b) Geological cross-section of the aquifer along profile A-A' using data from five exploration wells displayed in (a). The bedrock is made of limestone (yellow) and the aquifer unit's thicknesses atop decrease eastward.

3 Datasets and Methods

3.1. Datasets

3.1.1. SAR Data

Our analysis is based on 12 Envisat ASAR images of the AP acquired in StripMap (SM) mode, 14 ALOS-1 PALSAR images acquired in Fine Beam Single Polarization (FBS) and Fine Beam Double Polarization (FBD) modes, and 243 Sentinel-1 images acquired in Interferometric Wide-swath (IW) mode (Figure 1a). The Envisat descending, ALOS-1 ascending, and Sentinel-1 ascending and descending datasets were acquired with spatial resolutions of 8 × 4 m, 8 × 3 m, and 5 × 20 m (Range × Azimuth), respectively (Tables S3 and S4).

3.1.2. Hydrogeological and Weather Data

We use monthly data from 28 borehole piezometers to quantify groundwater level (GWL) variations from March 2003 to March 2020 (Figure 1a). We rely on an Inverse Distance Weighted (IDW) (Shepard, 1968) interpolation method to generate multi-annual GWL change maps (Figure S10). Logs of several exploration wells (Figure 1a; TAMAB (2004)) are used to derive lithological information from the upper approximately 100 m (Figure S8). Stratigraphic data of the AP are also derived from the geological map at a scale of 1:100,000 (Geological Survey of Iran, 1997).

We generate time series of monthly precipitation relying on the total precipitation parameter of the ECMWF Reanalysis v5 (ERA5)-Land hourly data (from the ERA5 climate reanalysis) to constrain weather data over the last decades at a resolution of $0.1^{\circ} \times 0.1^{\circ}$ (Figure S1a; Muñoz Sabater (2019)). We compute the cumulative precipitation departure (CPD) to enable comparisons with groundwater level changes (Figure S1a; Hanson et al. (2004)). We derive a time series of Land Surface Temperature (LST) using the MODIS/Terra product

MOD11_L2 swath that includes LST values and daily emissivity on a 1200 km × 1200 km grid with a resolution of 1 km (Figure S1b).

3.2. Methods

3.2.1. InSAR Approach

To track ground deformation over the period covered by each SAR data, we use the InSAR Computing Environment (ISCE) software and Small BAseline Subset (SBAS) time series method (Berardino et al., 2002) implemented in the Miami INsar Time-series software in PYthon (MintPy) (Yunjun et al., 2019). We rely on the 1-arcsec Digital Elevation Model (DEM) of the Shuttle Radar Topography Mission (SRTM; Jarvis et al. (2008)) to exclude topographical contributions. We resample the interferograms to 90 m for the Envisat and ALOS-1, and 30 m for the Sentinel-1 datasets to reduce the speckle noise and use SNAPHU for phase unwrapping (Chen and Zebker, 2003). We use mean spatial coherence thresholds of 0.7 and 0.8 (Figure S2) to eliminate outliers caused by unwrapping errors for the Envisat descending and ALOS-1 ascending datasets, respectively (Tizzani et al., 2007). We use the Python based Atmospheric Phase Screen (PyAPS) (Jolivet et al., 2014; Jolivet et al., 2011) and the ERA-5 weather model data with a spatial resolution of 31 km (Hersbach et al., 2020) to decrease tropospheric phase delay. We remove short-frequency signals in the form of a linear ramp to mitigate orbital and ionospheric artifacts. Finally, all datasets are referenced to a single stable point that presents high coherence (cross in Figure 2).

Assuming minimal contributions of horizontal motions to the line-of-sight (LOS) displacements, as confirmed with the Sentinel-1 ascending and descending datasets (Figure S6), we convert the LOS InSAR velocity maps (d_{LOS}) into the vertical motions (d_V) using the mean incidence angle value θ of each satellite ($d_V = \frac{d_{LOS}}{cos\theta}$). We convert the LOS InSAR velocity standard deviation maps (Std_{LOS}) into the vertical deformation standard deviation maps ($Std_V = \frac{Std_{LOS}}{cos\theta}$) to derive spatially variable uncertainties (Figure S4). Temporal uncertainties are calculated by averaging a window of 13 × 13 pixels at the reference point for each epoch of time series (Figure S5; Mirzadeh et al. (2021)).

184 3.2.2. Separation of Sources from Independent Component Analysis

185 To constrain the hydrological and geological control(s) on the spatiotemporal changes
186 and the transition from elastic to inelastic deformation in the AP, we use an ICA-based approach.
187 First, we resample the vertical time series of displacement derived from the Envisat descending,
188 ALOS-1 ascending, and Sentinel-1 ascending and descending dataset into 90m grids and apply
189 the method proposed by Chaussard and Farr (2019). We use a Principal Component Analysis
190 (PCA) to define how many independent components (ICs) can retain the signal and also their
191 order of importance (Cattell, 1966). We use 254,550 samples per date and 12, 14, 129, and 114
192 epochs for the Envisat descending, ALOS-1 ascending, and Sentinel-1 ascending and descending
193 datasets, respectively. Based on the PCA results, a single component explains 94.6%, 92.8%,
194 94.9%, and 97.2% of the eigenvalues for each dataset, respectively (increasing to 98.9%, 98.3%,
195 97.3%, and 98.6% when including the four components). Results for each IC are represented as
196 an eigenvalue time series to display the signal's magnitude at each epoch and a score map scaled
197 by the contribution of the retained components to the original data, showing the pixels
198 experiencing the observed eigenvalue time series (Figure S7). We consider the 2-sigma
199 spatiotemporal uncertainties of the InSAR results (2 × maximum of spatiotemporal uncertainties;
200 see section 3.2.1) as the threshold for all datasets to extract the spatial extent of significant
201 deformation. This threshold is then converted from cm/yr to eig/yr for each dataset:

$$threshold\ {}_{m}^{eig/yr} = \frac{threshold^{cm/yr}}{Scaled\_Score_m} \quad (1)$$

202 where $Scaled\_Score_m$ is a maximum score scaled with % eigenvalues explained by the
203 dominant IC for dataset m. These thresholds are used to mask the score maps so that changes in
204 the extent of deformation over time can be isolated (score values lower than the threshold are
205 masked). This approach is applied to the score map of the dominant component (IC1), which
206 captures inelastic deformation, to highlight the time-dependent extent of the area affected by
207 inelastic deformation.

4 Results and Analysis

4.1 Overview of Deformation

4.1.1 Spatio-temporal Patterns and Rates of Deformation

The multi-temporal analysis of deformation in the AP allows us to see the temporal changes in the patterns and rates of deformation. Figure 2 shows the mean vertical velocity maps converted from the mean LOS velocities (Figure S3), and reveals three major subsidence features in the AP. In terms of subsidence rates, the most significant feature is an elongated northwest-southeast zone referred to as the Main Subsidence Zone (MSZ), which covers an initial area of 37.4 km^2 with a rate ≥ 1.2 cm/yr (three-sigma maximum spatiotemporal uncertainties; Figure S4-5) in the Envisat dataset. The MSZ spatially expanded between the Envisat (2003-2005) and ALOS-1 (2006-2010) and Sentinel-1 (2015-2020) datasets and reaches 135 km^2 in Sentinel-1 ascending and descending datasets. In addition to the MSZ, a new deformation area appears in the ALOS-1 and Sentinel-1 datasets northwest of Abarkuh city (dark circle in Figure 2b-d) with a subsidence rate of 1.3 cm/yr. The profile A-A' (Figure 2) highlights the expansion of the MSZ toward the northwest between 2 and 8 km in both the ALOS-1 and Sentinel-1 datasets compared to the Envisat data. In the center of the MSZ, we observe an increase followed by a decrease in the subsidence rates by 3 & 2 cm/yr, respectively, between 9.5 and 15 km (shaded areas in Figure 3a). Figure 3b displays the subsidence rates and changes in the spatial extent of the zones of deformation north of Abarkuh city along the profile B-B'.

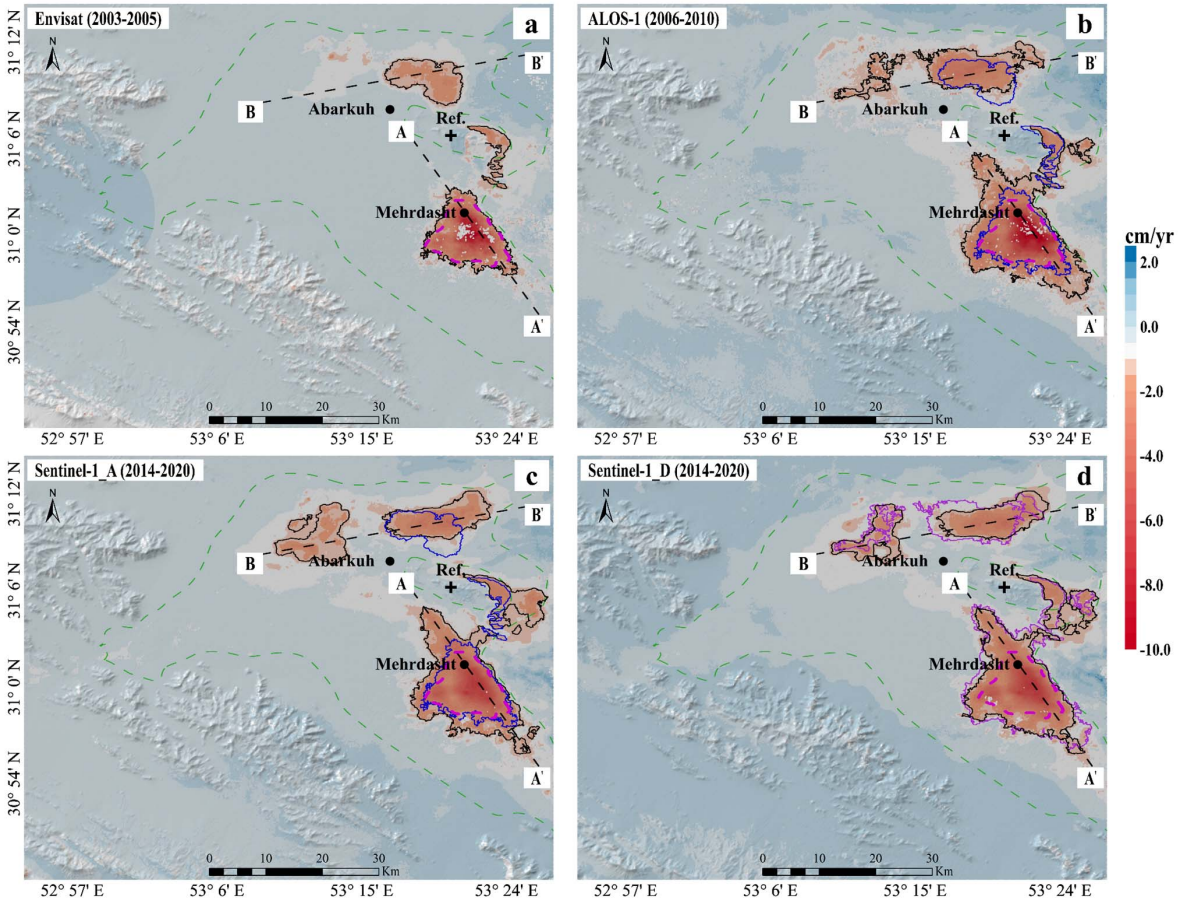

Figure 2. Annual mean vertical velocity maps, derived from the (a) Envisat, (b) ALOS-1, and (c)-(d) Sentinel-1 ascending and descending datasets, respectively. Red colors indicate zones of subsidence and white to light-blue colors indicate the areas with little or no displacement. Black circles indicate the major cities, and black dashed lines display the positions of the two profiles $(B-B')$ and $(A-A')$ shown in Figure 3. The green dashed-lines polygon in (a)-(d) indicates the AP aquifer boundary. Black contours indicate the extent of subsiding areas with a rate of $\geq$ 1.2 cm/yr in each dataset. Pink dashed-lines highlight the Envisat boundary of the Main Subsidence Zone (MSZ). Blue contours in (b)-(c) and purple contours in (d) mask the extent of the Envisat and ALOS-1 subsiding areas overlaying the ALOS-1 and Sentinel-1 observations. The cross (Ref.) marks the reference pixel located in the stable area.

228

229 4.1.2 Uncertainties and Consistency Assessment

230 We investigate the uncertainties and consistency of the mean vertical velocities from the
231 Envisat, ALOS-1, and Sentinel-1 ascending and descending datasets. Figure S4 shows that
232 spatial uncertainties of velocity are mostly less than 4 mm/yr over the entire study area with
233 means of 1.1 and 1.6 mm/yr for the Envisat and ALOS-1 datasets, respectively. In the Sentinel-1
234 ascending and descending data, spatial uncertainties are less than 1 mm/yr with respective means

of 0.4 and 0.3 mm/yr. Figure S5 shows that the majority of epochs have uncertainties < 2 mm in all datasets, with the exception for three epochs (Figure S5b-c), likely contaminated by atmospheric turbulences (Yunjun et al., 2019).

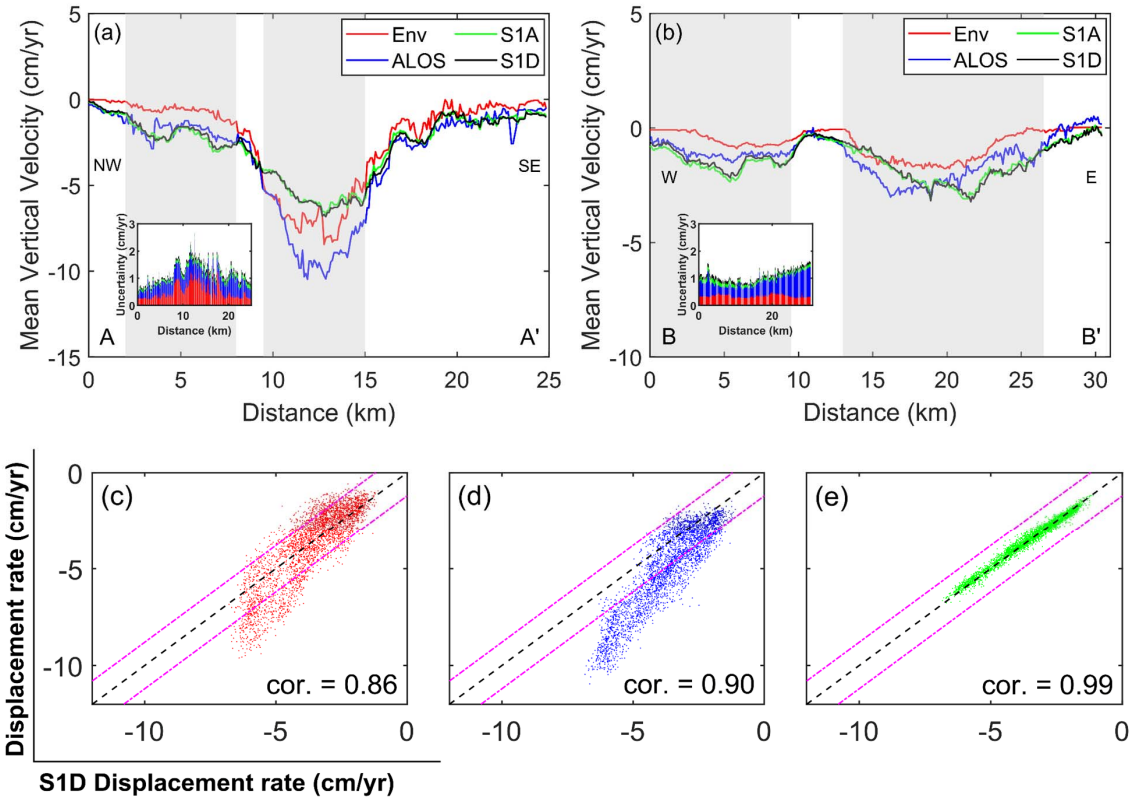

Figure 3. Mean vertical deformation rates, derived from the Envisat (red), ALOS-1 (blue), and Sentinel-1 descending (black) and ascending (green) datasets along $(A-A')$ (a) and $(B-B')$ (b) profiles (positions displayed in Figure 2). Insets show the corresponding 3-sigma uncertainties. The shaded parts highlight the locations of substantially different subsidence rate in the Envisat, ALOS-1, and Sentinel-1 ascending and descending datasets. Lateral expansion of the subsiding areas is visible along both profiles. (c-e) Comparisons of the mean vertical velocities derived for resampled common points in a 90 m grid within the MSZ (pink dashed-lines in Figure 2a). The Sentinel-1 descending mean vertical velocity is used as reference and compared to the (c) Envisat, (d) ALOS-1, and (e) Sentinel-1 ascending dataset. The dashed black and dashed-dotted pink lines in (c-e) show identical vertical displacement rates and a 3-sigma range of ±1.2 cm/yr, respectively. (c) to (e) display that the subsidence rates from the Envisat, ALOS-1, and Sentinel-1 ascending datasets are highly correlated with the Sentinel-1 descending data. (e) confirms the absence of major horizontal deformation in the Sentinel-1 dataset.

Mean deformation rate uncertainties along the profiles are shown in the inset of Figures 3a & 3b. Sentinel-1 has the smallest mean uncertainties (1.1 mm/yr) in both ascending and

descending datasets. Envisat and ALOS-1 have mean uncertainties of approximately 3.4 and 5.7 mm/yr along the B-B' profile, respectively but the same mean uncertainty of approximately 5.1 mm/yr along the A-A' profile (see Figure S4 for maps of estimated sigma uncertainties).

We compare the mean vertical velocities derived for resampled common points in a 90 m grid within the MSZ (pink dashed-lines in Figure 2a) from the four time series with the Sentinel-1 descending dataset being used as reference (Figure 3c-e). Correlation coefficients between the displacement rates of the Sentinel-1 descending and other datasets range between 0.86 and 0.99, demonstrating a good consistency. The agreement between Sentinel-1 ascending and descending data supports the assumption of no significant horizontal motion in the MSZ. Envisat data show the lowest correlation to the Sentinel-1 descending data (0.86), likely due to the different temporal coverage of the datasets and temporal changes in the subsidence rates. Specifically, significantly different subsidence rates are also observed between 9.5 and 15 km, at the MSZ boundary on the A-A' profile (Figure 3b) when comparing the Envisat and Sentinel-1 data.

4.2 Multi-Temporal Inelastic Compaction

Groundwater pumping lowers water levels and decreases pore water pressure in an aquifer system, increasing the effective stress. When the hydraulic head drops below the previous lowest level, inelastic deformation happens due to permanently collapsing pore spaces, especially in fine grained aquitards which are more compressible than coarse-grained aquifer layers (Meade, 1964; Wilson and Gorelick, 1996). Since pumping rate is spatiotemporally inhomogeneous and sediment properties vary spatially, elastic and inelastic contributions of deformation change spatially over time. To explore the time and space variations of inelastic and elastic deformations, we apply the ICA to the time series derived from the Envisat, ALOS-1 and Sentinel-1 ascending and descending (Figure S7).

The first component (IC1) retains 94.6%, 92.8%, 94.9%, and 97.2% of the eigenvalues for the Envisat, ALOS-1, and Sentinel-1 ascending and descending datasets, respectively, and displays a spatial pattern similar to the mean deformation rate maps of all datasets (Figures 2 and S7). Each of its eigenvalues time series shows a nearly linear trend with slopes of -0.55, -0.85, -0.61, and -0.65 eigenvalues/year (-9.12, -10.22, -6.42, and -6.67 in cm/yr) for the Envisat, ALOS-1, and the Sentinel-1 ascending and descending datasets, respectively (Figures 4e-h and S7).

Together, the other components (IC2-4) explain 4.3%, 5.5%, 2.3%, and 1.4% of the eigenvalues for the Envisat, ALOS-1, and Sentinel-1 ascending and descending datasets, respectively. IC2 shows positive score values limited to the northeast of the MSZ for the ALOS-1 data and a noisy signal (mix of positive and negative scores) within the MSZ for the Envisat data. IC2 explains 2.5%, 2.6%, 0.9%, and 0.8% of the eigenvalues and has an eigenvalues time series with a slight descending trend and slopes of -0.01, -0.09, -0.09, and -0.18 (in eigenvalues/year) for the Envisat, ALOS-1, and Sentinel-1 ascending and descending datasets, respectively. IC3 shows no clear pattern in the score maps for the ALOS-1, and Sentinel-1 ascending and descending datasets, but has positive score values north of the MSZ in the Envisat data (retaining retains 1.3% of the eigenvalues), with the eigenvalues time series slope of -0.22 (in eigenvalues/year). The fourth component (IC4) score map shows a correlated zone in the northeastern zone of subsidence in the Envisat and ALOS-1 datasets and in the northwestern zone of the subsidence in the Sentinel-1 ascending and descending dataset with eigenvalues time series with slight downward trends with slopes of -0.16, -0.07, -0.18, and -0.07 eig/yr for the Envisat, ALOS-1, and Sentinel-1 ascending and descending datasets, respectively.

Based on its linear eigenvalue time series (Figure S7), we consider that the IC1 highlights inelastic deformation. The other components (IC2-4) show long-wavelength spatial signals with low-amplitude eigenvalues, suggesting that they are likely to capture the noise, possibly reflecting orbital errors and ionospheric delays.

Figure 4 shows the spatiotemporal patterns of the IC1 (score maps) that highlight inelastic deformation. The growth in the extent of the IC1 positive score over time is clearly visible around the MSZ and two additional zones to the north between the Envisat and Sentinel-1 periods. As shown in Figures 4e-h and S7, the eigenvalues time series of the IC2 component, derived from all datasets, reveal no clear signal of seasonal elastic deformation during the study period, suggesting that the inelastic deformation captured by IC1 dominates. The eigenvalues time series results also reveal that the rate of the IC1 component decreases between the Envisat and Sentinel-1 observation periods, with a peak occurring during the 2006-2010 period imaged by ALOS-1 (Figure 4b and 4f).

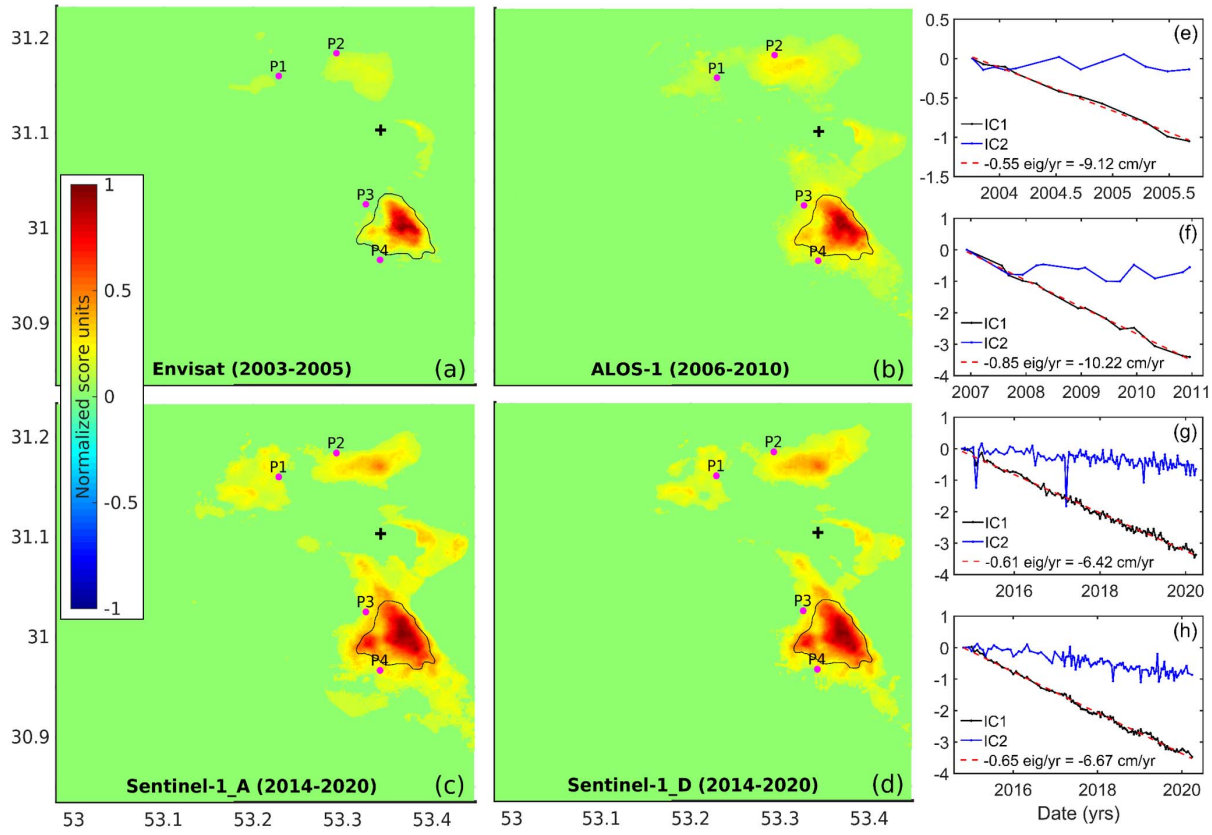

Figure 4. (a-d) Score maps of the IC1 component derived from the (a) Envisat, (b) ALOS-1, and (c)-(d) Sentinel-1 ascending and descending time series of inferred vertical motions. The cross marks the reference point placed in a stable area. The black polygon displays the boundary of the MSZ. Pink circles indicate the locations of exploration wells. (e-h) Eigenvalues time series of the IC2 (blue) and IC1 (black) components, derived from the (e) Envisat, (f) ALOS-1, and (g)-(h) Sentinel-1 ascending and descending datasets. The red dash lines show the best-fit linear regression of the IC1.

4.3 Potential Causes

GWL changes in the aquifer over 33 years (1984–2016) (Figure 5c) manifest a mean 20 m drop with ~ 1147 million cubic meters (MCM) of groundwater lost. This shows the severe stress has been imposed on the groundwater system, resulting in storage depletion and driving inelastic deformation in the fine-grained sediments layers (see Figures 1b and S8) (Iran's WRM Co., 2014).

To evaluate the controls on the inelastic deformation pattern, we combine the score maps of the IC1 component (Figure 4a-d) assuming that the recovery process from inelastic deformation cannot happen in a short period (e.g., 2-3 years) but areas with elastic deformation

311 can transition to experiencing inelastic deformation (Ireland et al., 1984). We also rely on the
312 spatiotemporal behavior of GWL changes (Figure S10) and the lithology data from the
313 exploration wells (Figure S8) located inside the boundary of the inelastic deformation (see the
314 locations in Figure 5a). Figure 5a shows the overlap of the IC1 score maps from different
315 datasets. Red colors highlight areas of long-term inelastic deformation during all three
316 observation periods. Light-blue colors highlight the growth in the extent of inelastic deformation
317 (IC1) captured by the Envisat to ALOS-1 data, referred to as Expansion(A). Dark blue colors
318 highlight the expansion of the zone of inelastic deformation between the ALOS-1 to Sentinel-1
319 periods, referred to as Expansion(S).

320 Over time, the inelastic deformation has expanded to areas outside of the MSZ to the
321 north of the AP. The maximum expansion in inelastic deformation is Expansion(A) (light-blue in
322 Figure 5a) with 119 km^2. The zone of long-term inelastic deformation (red in Figure 5a) and
323 Expansion(S) (dark-blue in Figure 5a) are estimated at 90.4 and 24.2 km^2, respectively. Figure
324 5b displays time series of the meanvariance (mean – 2 × standard deviation) of GWL changes
325 determined from piezometers (Figure S10) across (1) the area of long-term inelastic deformation
326 (red in Figure 5a), (2) the zones of Expansion(A), and (3) the area of Expansion(S). The slope of
327 the meanvariance of the GWL changes of Expansion(A) (light-blue curve in Figure 5b) is 25%
328 greater than the long-term slope (red in Figure 5b), suggesting that more fine-grained sediments
329 (clay layers) have been drained (Figure S8c-d). Figure 5b also shows that since 2014, the slope
330 of Expansion(S) (blue curve) is 26% greater than the long-term trend (red curve), suggesting a
331 larger drop in the GWL in the Expansion(S) area than the long-term inelastic deformation.

332 The lithology data from the four explorations wells is shown in Figure S8. To simplify
333 interpretations, we rely on wells located in the long-term inelastic deformation zones (P2), the
334 Expansion(A) zone (P3 and P4) and the Expansion(S) zone (P1). At P2, thick (>63 m) drained
335 clays are observed, likely accommodating the inelastic deformation observed during the Envisat,
336 ALOS-1, and Sentinel-1 periods despite GWL seasonality (Figure S9b). At P3 and P4, 3 m of
337 clays have been drained during the Envisat period (Figure S8c-d) due to an acceleration in the
338 GWL decline (light blue curve in Figure 5b), which likely initiated the inelastic deformation
339 observed in the ALOS-1 data. Finally, at P1, while gravel and sands layers likely continue to
340 deform elastically, the clay layers is drained by an additional 5 m between the Envisat and

Sentinel-1 time period (29 to 34 m), likely initiating inelastic deformation once a stress threshold is reached in the clay.

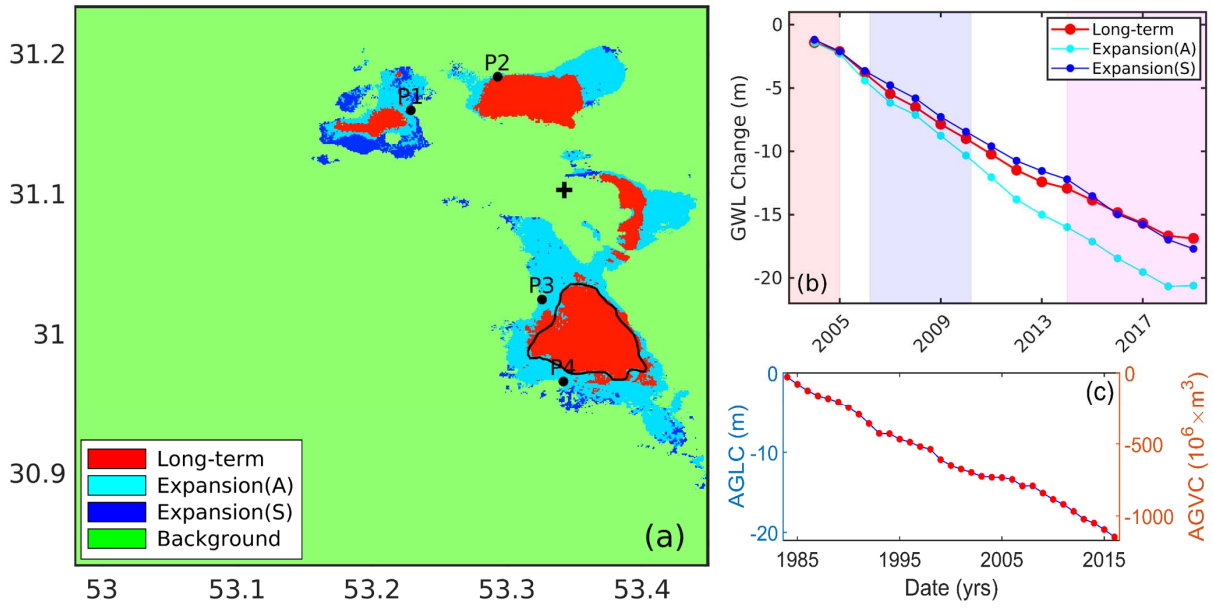

Figure 5. (a) Spatial extent of inelastic deformation in the AP derived from the Envisat, ALOS-1, and Sentinel-1 ascending and descending datasets. Red color indicates the long-term inelastic deformation in common between the four datasets. Light-blue and dark-blue colors indicate the Expansion(A) (Envisat to ALOS-1) and the Expansion(S) (ALOS-1 to Sentinel-1), respectively. The cross shows the reference point placed in a stable area. Black circles specify the locations of exploration wells. The black polygon displays the boundary of the Main Subsidence Zone. (b) Time series of the meanvariance (mean – 2 × standard deviation) of GWL changes (m), considering 2003 as the reference year for three classes defined in (a). The red, blue, and pink shaded time-spans show the Envisat, ALOS-1, and Sentinel-1 observation periods, respectively. (c) Average yearly accumulated groundwater level changes (AGLC) in meters (on left y-axis) and the total yearly accumulated groundwater volume changes (AGVC) in million cubic meters (on right y-axis) between 1984 and 2016 provided by the Iran's WRM Co. (2014).

4.4 "Hidden" Short-Term Elastic Deformation

A slight seasonality in IC1 eigenvalues time series of Sentinel-1 ascending and descending datasets, especially after 2017 (Figure 4g-h), suggests the potential existence of elastic component mixed with the inelastic deformation. We probe the characteristics of this seasonality by (1) fitting a linear regression to the IC1 eigenvalues time series and (2) applying Singular Spectrum Analysis (SSA) to the residuals (Figures 6b and S11b) (Vautard et al., 1992). The residuals of Sentinel-1 ascending and descending dataset (Figure 6c and S11c) are in phase

with each other but have time-variable amplitude. In contrast, a one-month time lag is observed between this seasonal signal in IC1 time series and average groundwater level changes (AGLC), estimated with autocorrelation in Hydrologic and Climatic Analysis Toolkit (HydroClimATe; Dickinson et al. (2014)) (Figure 6e). Water level changes occurring one month in advance of the seasonal deformation suggest that the seasonal fluctuations in groundwater level induce the residual seasonal deformation observed in IC1. This suggests that even with inelastic deformation dominating, the aquifer system is still reacting to fluctuating seasonally-driven pumping rates at wells (Table S2). Elastically deforming coarse-grained layers are responsible for this seasonal deformation signal in response to fluctuating extraction rates, which occurs collocated and concurrent with inelastic deformation in clay layers.

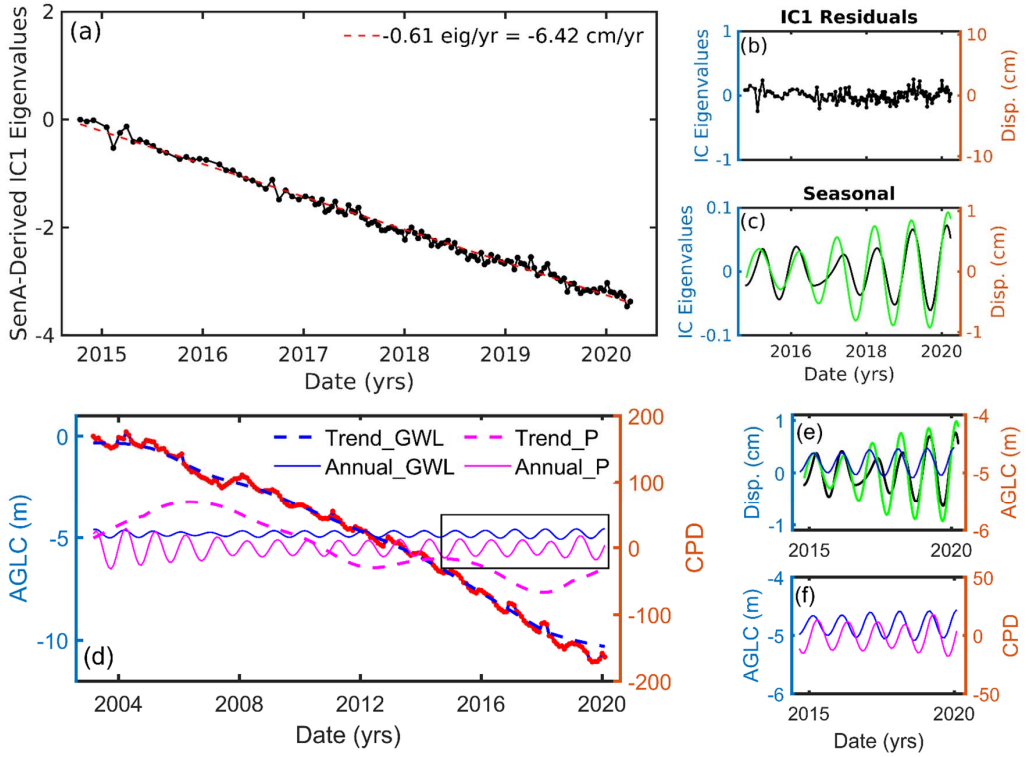

Figure 6. (a) IC1 eigenvalues time series of the Sentinel-1 ascending dataset. The red dash line show the best-fit linear regression of the IC1 component. (b) Residual of the IC1 eigenvalues time series and the best-fit linear regression. (c) Seasonal component of the residual time series extracted using the SSA-MTM Toolkit (Vautard et al., 1992). (d) Average yearly groundwater level changes (AGLC, red curve) in meters between 1984 and 2016 (Iran's WRM Co., 2014). The blue dashed and full lines indicate the multi-year trend and seasonal signal of the AGLC, respectively. The pink dashed and full lines show the multi-year trend and seasonal signal of the cumulative precipitation departure (CPD) from Figure S1. The black box demonstrates the time window for which the GWL and CPD time series overlap with the IC1 eigenvalues time series of Sentinel-1 datasets. (e) Close-up view of the seasonal component of the AGLC (blue) and the seasonal component of the residual time series of Sentinel-1 ascending (black) and descending (green) datasets. (i) Close-up view of the seasonal component of the AGLC (blue) and the CPD (pink). Time series of residual and seasonal components are both represented in eig. (left y-axis) and cm (right y-axis) in (b)-(c).

5 Discussion

To develop sustainable aquifer protection plans and assess the impact of current pumping practices, it is critical to quantify the spatially-variable onset of inelastic deformation. In the AP, the majority of the land subsidence currently observed is inelastic (irrecoverable) and captured by a single component (IC1). The low-frequency spatial signals observed in other components (IC2-4) suggest that they capture noise, including ionospheric delay and orbital errors. The extent of the areas experiencing inelastic deformation has significantly increased over the past two decades, highlighting that we are now at or near a tipping point in time between sustainability and permanent damage to our underground water resources.

Lithologic and hydrologic data suggest that the temporal evolution of the extent of the area affected by inelastic compaction is controlled by the thickness of the drained clays. These results are similar to those reported in the Salmas Plain., Iran (Shahbazi et al., 2022) where the relationship between an acceleration in depletion of aquifer storage and inelastic subsidence driven by compaction of fine-grained units was discovered. Time series of the GWL changes across the area experiencing inelastic deformation show an acceleration in the rate of groundwater decline, which causes the growth of the areas affected by inelastic deformation over time. Once groundwater levels reach a new low, inelastic deformation is initiated, driven by the stress in the drained clay layers exceeding the pre-consolidation stress.

The Singular Spectrum Analysis (SSA) applied to the Sentinel-1 IC1 eigenvalue time series suggests that the deformation has a modest elastic response to seasonal fluctuations in

pumping rates even when inelastic deformation dominates. These observations show that geodetic data capture the sum of the deformation processes occurring from the surface to the stable substrate at a given location, and elastic deformation may concurrently happen in the coarse-grained sediments layers while inelastic deformation occurs in the fine-grained sediments layers. Therefore, decomposition of the resulting deformation signal is necessary to isolate each process.

Our work highlights (1) the need to revise current pumping practice to protect groundwater resources in Central Iran, (2) the potential of using InSAR to evaluate the sustainability of such current practices, and (3) the necessity to consider the spatial and temporal correlation of processes causing ground deformation when interpreting InSAR mean velocity maps.

6 Conclusions

A 2003-2020 InSAR multi-sensor time series analysis shows an elongated northwest-southeast zone of land subsidence in the AP with covering a maximum area of ~ 135.1 km^2. The ICA of the InSAR dataset reveals that the majority of the observed subsidence is inelastic and therefore irreversible. The areas experiencing inelastic deformation have substantially expanded over time as a result of groundwater levels locally reaching new lows, which result in clays experiencing stress exceeding the pre-consolidation stress. The high temporal sampling of the Sentinel-1 dataset (6 days) enables detecting small magnitude seasonal deformation, which shows that the aquifer reacts elastically to fluctuations in the groundwater levels. These observations confirm that elastic deformation may occur concurrently to inelastic deformation and the observed surface deformation is the result of multiple processes occurring at the same place at the same time. Our results highlight that we are near a tipping point in time between sustainability and permanent damage to our underground water resources in Iran, emphasizing the fast that current decisions have the potential to change the natural resources landscape permanently.

Data Availability Statement

The geological and hydrogeological data (i.e., piezometers, logs of exploration wells, and pumping wells) are accessible by contacting the Geological Survey and Mineral Explorations of Iran (GSI) and the Regional Water Company of Yazd, respectively. The Envisat and Sentinel-1 datasets are copyrighted by the European Space Agency (ESA) and freely available through the

ESA archive and the Alaska Satellite Facility (ASF) archive. The ERA5 and Shuttle Radar Topography Mission (SRTM) DEM datasets are provided through the Copernicus Climate Data Store and the NASA's Land Processes Distributed Active Archive Center (LP DAAC), located at USGS Earth Resources Observation and Science (EROS) Center, respectively. LST dataset are accessible from the Data Catalog of the Google Earth Engine. The InSAR Computing Environment (ISCE) software, Miami INsar Time-series software in PYthon (MintPy), and Python 3 Atmospheric Phase Screen (PyAPS) are available in (https://github.com/isce-framework/isce2), (https://github.com/insarlab/MintPy), and (http://earthdef.caltech.edu/#), respectively. The InSAR results of the work, including the time series of deformation and mean velocity maps, are accessed in a public repository through the following link (https://doi.org/10.5281/zenodo.5972151).

Acknowledgments

The Strategic Priority Research Program Project of the Chinese Academy of Sciences (Grant No. XDA23040100) and the CAS-TWAS President's Fellowship supported this research. The Japan Aerospace Exploration Agency (JAXA) provided ALOS data within RA6 (PI 3059). The authors thank the Regional Water Company of Yazd, Iran's Water Resources Management Company, and Geological Survey & Mineral Exploration of Iran (GSI) for the hydrogeological and geological information of the AP.

References

Amelung, F., Galloway, D. L., Bell, J. W., Zebker, H. A., and Laczniak, R. J.: Sensing the ups and downs of Las Vegas: InSAR reveals structural control of land subsidence and aquifer-system deformation, Geology, 27, 483-486, 1999.

Berardino, P., Fornaro, G., Lanari, R., and Sansosti, E.: A new algorithm for surface deformation monitoring based on small baseline differential SAR interferograms, IEEE Transactions on geoscience and remote sensing, 40, 2375-2383, 2002.

Bürgmann, R., Rosen, P. A., and Fielding, E. J.: Synthetic aperture radar interferometry to measure Earth's surface topography and its deformation, Annual review of earth and planetary sciences, 28, 169-209, 2000.

Cattell, R. B.: The scree test for the number of factors, Multivariate behavioral research, 1, 245-276, 1966.

Chaussard, E., Bürgmann, R., Shirzaei, M., Fielding, E. J., and Baker, B.: Predictability of hydraulic head changes and characterization of aquifer-system and fault properties from InSAR-derived ground deformation, Journal of Geophysical Research: Solid Earth, 119, 6572-6590, 2014.

Chaussard, E. and Farr, T. G.: A new method for isolating elastic from inelastic deformation in aquifer systems: application to the San Joaquin Valley, CA, Geophysical Research Letters, 46, 10800-10809, 2019.

Chaussard, E., Havazli, E., Fattahi, H., Cabral-Cano, E., and Solano-Rojas, D.: Over a Century of Sinking in Mexico City: No Hope for Significant Elevation and Storage Capacity Recovery, Journal of Geophysical Research: Solid Earth, n/a, e2020JB020648, 2021.

Chaussard, E., Milillo, P., Bürgmann, R., Perissin, D., Fielding, E. J., and Baker, B.: Remote sensing of ground deformation for monitoring groundwater management practices: Application to the Santa Clara Valley during the 2012–2015 California drought, Journal of Geophysical Research: Solid Earth, 122, 8566-8582, 2017.

Chen, C. and Zebker, A.: SNAPHU: statisticalcost, network-flow algorithm for phase unwrapping, Retrieved April, 27, 2016, 2003.

Dickinson, J. E., Hanson, R. T., and Predmore, S. K.: HydroClimATe: Hydrologic and climatic analysis toolkit, US Department of the Interior, US Geological Survey Reston, VA, USA, 2014.

Ezquerro, P., Herrera, G., Marchamalo, M., Tomás, R., Béjar-Pizarro, M., and Martínez, R.: A quasi-elastic aquifer deformational behavior: Madrid aquifer case study, Journal of Hydrology, 519, 1192-1204, 2014.

Geological Survey of Iran: https://gsi.ir/en, last access: 15 November 2019, 1997.

462 Gualandi, A. and Liu, Z.: Variational Bayesian Independent Component Analysis for InSAR Displacement Time-
463 Series With Application to Central California, USA, Journal of Geophysical Research: Solid Earth, 126,
464 e2020JB020845, 2021.
465 Guzy, A. and Malinowska, A. A.: State of the art and recent advancements in the modelling of land subsidence
466 induced by groundwater withdrawal, Water, 12, 2051, 2020.
467 Hanson, R., Newhouse, M., and Dettinger, M.: A methodology to asess relations between climatic variability and
468 variations in hydrologic time series in the southwestern United States, Journal of Hydrology, 287, 252-269, 2004.
469 Hersbach, H., Bell, B., Berrisford, P., Hirahara, S., Horányi, A., Muñoz-Sabater, J., Nicolas, J., Peubey, C., Radu,
470 R., and Schepers, D.: The ERA5 global reanalysis, Quarterly Journal of the Royal Meteorological Society, 146,
471 1999-2049, 2020.
472 Hoffmann, J., Galloway, D. L., and Zebker, H. A.: Inverse modeling of interbed storage parameters using land
473 subsidence observations, Antelope Valley, California, Water Resources Research, 39, 2003.
474 Iran's WRM Co.: http://wrbs.wrm.ir/, last access: 15 November 2019, 2014.
475 Ireland, R. L., Poland, J. F., and Riley, F. S.: Land subsidence in the San Joaquin Valley, California, as of 1980, US
476 Government Printing Office, 1984.
477 Jarvis, A., Reuter, H., Nelson, A., and Guevara, E.: Hole-Filled Seamless SRTM Data V4: International Centre for
478 Tropical Agriculture (CIAT): http, srtm. csi. cgiar. org, accessed, 31, 2008.
479 Jolivet, R., Agram, P. S., Lin, N. Y., Simons, M., Doin, M. P., Peltzer, G., and Li, Z.: Improving InSAR geodesy
480 using global atmospheric models, Journal of Geophysical Research: Solid Earth, 119, 2324-2341, 2014.
481 Jolivet, R., Grandin, R., Lasserre, C., Doin, M. P., and Peltzer, G.: Systematic InSAR tropospheric phase delay
482 corrections from global meteorological reanalysis data, Geophysical Research Letters, 38, 2011.
483 Lu, Z. and Danskin, W. R.: InSAR analysis of natural recharge to define structure of a ground-water basin, San
484 Bernardino, California, Geophysical Research Letters, 28, 2661-2664, 2001.
485 Meade, R. H.: Removal of water and rearrangement of particles during the compaction of clayey sediments, US
486 Government Printing Office, 1964.
487 Miller, M. M. and Shirzaei, M.: Spatiotemporal characterization of land subsidence and uplift in Phoenix using
488 InSAR time series and wavelet transforms, Journal of Geophysical Research: Solid Earth, 120, 5822-5842, 2015.
489 Mirzadeh, S. M. J., Jin, S., Parizi, E., Chaussard, E., Bürgmann, R., Delgado Blasco, J. M., Amani, M., Bao, H., and
490 Mirzadeh, S. H.: Characterization of Irreversible Land Subsidence in the Yazd-Ardakan Plain, Iran From 2003 to
491 2020 InSAR Time Series, Journal of Geophysical Research: Solid Earth, 126, e2021JB022258, 2021.
492 Muñoz Sabater, J.: ERA5-Land hourly data from 1981 to present, Copernicus Climate Change Service (C3S)
493 Climate Data Store (CDS), 10, 2019.
494 Ojha, C., Werth, S., and Shirzaei, M.: Groundwater loss and aquifer system compaction in San Joaquin Valley
495 during 2012–2015 drought, Journal of Geophysical Research: Solid Earth, 124, 3127-3143, 2019.
496 Pavelko, M. T.: Estimates of hydraulic properties from a one-dimensional numerical model of vertical aquifer-
497 system deformation, Lorenzi Site, Las Vegas, Nevada, US Department of the Interior, US Geological Survey, 2004.
498 Pepe, A. and Calò, F.: A review of interferometric synthetic aperture RADAR (InSAR) multi-track approaches for
499 the retrieval of Earth's surface displacements, Applied Sciences, 7, 1264, 2017.
500 Poland, J. F. and Ireland, R.: Land subsidence in the Santa Clara Valley, California, as of 1982, Department of the
501 Interior, US Geological Survey, 1988.
502 Rezaei, A. and Mousavi, Z.: Characterization of land deformation, hydraulic head, and aquifer properties of the
503 Gorgan confined aquifer, Iran, from InSAR observations, Journal of Hydrology, 579, 124196, 2019.
504 Riley, F. S.: Mechanics of aquifer systems—The scientific legacy of Joseph F. Poland, 1998, 13-27.
505 Shahbazi, S., Mousavi, Z., and Rezaei, A.: Constraints on the hydrogeological properties and land subsidence
506 through GNSS and InSAR measurements and well data in Salmas plain, northwest of Urmia Lake, Iran,
507 Hydrogeology Journal, 30, 533-555, 2022.
508 Shepard, D.: A two-dimensional interpolation function for irregularly-spaced data, 1968, 517-524.
509 Shi, X., Fang, R., Wu, J., Xu, H., Sun, Y., and Yu, J.: Sustainable development and utilization of groundwater
510 resources considering land subsidence in Suzhou, China, Engineering geology, 124, 77-89, 2012.
511 TAMAB: National Groundwater Resources Status, Basic Studies Office, Iran Water Resources Management
512 Company, 2004.
513 Tizzani, P., Berardino, P., Casu, F., Euillades, P., Manzo, M., Ricciardi, G., Zeni, G., and Lanari, R.: Surface
514 deformation of Long Valley caldera and Mono Basin, California, investigated with the SBAS-InSAR approach,
515 Remote Sensing of Environment, 108, 277-289, 2007.
516 Vautard, R., Yiou, P., and Ghil, M.: Singular-spectrum analysis: A toolkit for short, noisy chaotic signals, Physica
517 D: Nonlinear Phenomena, 58, 95-126, 1992.

518 Wilson, A. M. and Gorelick, S.: The effects of pulsed pumping on land subsidence in the Santa Clara Valley,
519 California, Journal of hydrology, 174, 375-396, 1996.
520 Yunjun, Z., Fattahi, H., and Amelung, F.: Small baseline InSAR time series analysis: Unwrapping error correction
521 and noise reduction, Computers & Geosciences, 133, 104331, 2019.
522